High-quality WS_2 film as Hole Transport Layer in High-efficiency Non-fullerene Organic Solar Cells

Xiaojing Wang,‡[a] Peng Liu,‡[a] Boonkar Yap,[a,c,d] Ruidong Xia,[a] Wai-Yeung Wong,[b] Zhicai He*[a]

The liquid-exfoliated 2D transition metal disulfides (TMDs) are potential substitutes for Poly(3,4-ethylenedioxythiophene): poly(styrenesulfonate) (PEDOT: PSS) as the hole transport layers (HTLs) in Organic Solar Cells (OSCs). Herein, high-yield and high-quality WS2 flake layers are prepared by comprehensively controlling the initial concentration, sonication processing time and centrifugal speed. The WS2 layers deposited on in-situ transparent indium tin oxide (ITO) without plasma treatment show higher uniformity and conductivity than that formed on ITO after plasma treatment. With significant increase in the short-circuit current density (***JSC***), the power conversion efficiency (PCE) of PM6:Y6-based Non-fullerene OSCs using optimized WS2 as the HTL is higher than that using PEDOT: PSS as the HTL(15.75 % vs 15.31 %). Combining morphology characteristics with carrier recombination characteristics, the higher quality of the ITO/WS2 composite substrate leads to better charge transport and lower bimolecular recombination rate in the OSCs, thereby improving device performance.

a. State Key Laboratory of Luminescent Materials and Devices, Institute of Polymer Optoelectronic Materials and Devices, International School of Advanced Materials, School of Material Science and Engineering, South China University of Technology, Guangzhou, Guangdong, 510640, China. E-mail: zhicaihe@scut.edu.cn

b. Department of Applied Biology and Chemical Technology, The Hong Kong Polytechnic University (PolyU), Hung Hom, Hong Kong, 999077, China

c. Electronic and Communications Department, College of Engineering, Universiti Tenaga Nasional, Kajang, Selangor 43000, Malaysia

d. Institute of Sustainable Energy, Universiti Tenaga Nasional, Kajang, Selangor 43000, Malaysia

Introduction

A promising option to solve the fossil energy crisis and environmental pollution is to develop photovoltaic technology that directly uses solar energy to generate electricity. Due to the unique advantages of large-scale manufacturing through roll- to-roll printing processes, mechanical flexibility, translucency, and diverse applications, OSCs have attracted great interest in both academic institutions and industries in the past few decades.[1,2] The PCE of organic solar cells has rapidly increased to over 18% recently.[3-8] The great improvement of device performance is attributed to both the development of new materials and great achievements in device engineering.[9-14] The interfacial engineering between the active layer and the electrodes is one of the useful and feasible ways to improve carrier transport and extraction, thereby achieving high performances in OSCs.[15-19] There are numerous effective choices such as polyelectrolytes,[20] metal oxides(ZnO),[21] metal salts(LiF),[22] and composite interface materials,[23,24] etc. for electron-transport layers (ETLs) which modify the surface properties of the cathode. Poly(3,4-ethylenedioxythiophene): poly (styrenesulfonate) (PEDOT:PSS) has been widely

used to work as HTL in OSCs due to its advantages including good electrochemical / thermal stability, excellent optical transparency and high quality film formation.[25-27] However, the high hygroscopicity and acidity of PEDOT: PSS lead to the degradation of ITO as well as affect the conductivity and work function (WF) of the electrode.[28,29] Some efforts have been reported in published works to overcome the above shortcomings to a certain extent, such as the addition of surfactants or inorganic additives to PEDOT: PSS.[30,31] Meanwhile, many alternative HTL materials with excellent performance have also been explored, such as V_2O_5, WO_3 and other transition metal oxides.[32] However, the complex manufacturing processes such as high-temperature annealing and vacuum thermal evaporation limit the further development and application of transition metal oxides as HTLs.

On the other hand, due to potentially high carrier mobility and excellent optical transparency, low-dimensional transition metal disulfides are considered to be excellent anode modification layers in OSCs.[33] WS_2 is one of the representatives with superior performance. In the top-down methods, the most common method of thin film preparation is to peel off the WS_2 flakes by ultrasonication treatment.[34] The properties of the underlying substrate (such as composition or charge traps) are found to affect the film quality of 2D materials (such as graphene sheets).[35] Some methods are also applied to improve the characteristics of the substrate such as hydrogen plasma, oxygen plasma, vacuum plasma and pressure treatment,[36-39] thereby affecting the morphology and optical properties of the film on such substrates. Therefore, controlling and understanding nano-morphological changes of the low- dimensional transition metal disulfides during the process is a classic problem of surface engineering and is crucial to improve the performance of the interlayer in OSCs.[40] However, it is still challenging to control the yield, the film morphology and uniformity of the solution-processed WS_2 flakes layers to promote the work function tuning effect and charge transport in OSCs.

In this work, high-yield multilayer WS_2 flakes are prepared by comprehensively controlling the initial concentration before centrifugation, sonication processing time and centrifugal speed to form high-quality HTLs on ITO to replace PEDOT: PSS. The influence of the plasma treatment of ITO substrate on the consistency of the WS_2 film is also studied by atomic force microscopy (AFM), field emission scanning electron microscopy (FESEM), transmission electron microscopy (TEM) measurements and the grazing incident wide-angle X-ray scattering (GIWAXS) measurements. The Non-fullerene OSCs based on PM6:Y6 with the optimized WS_2 interlayer as HTLs achieve a high PCE of 15.75 %, which is about 18 % higher than that of the OSCs with WS_2 prepared without optimization processes (13.35 % vs 15.75 %), and even higher than that with PEDOT: PSS as HTL. The enhanced device performance is attributed to the improved uniformity and charge transport ability of the WS_2 HTLs as confirmed by a series of photoelectric technologies, thereby improving the carrier collection efficiency and reducing bimolecular recombination losses in OSCs. It is further found that WS_2 flakes are more likely to adhere to ITO substrate without plasma treatment and exhibit high-quality film properties.

Results and Discussion

Film characteristics

The water-soluble WS_2 nanosheets are prepared by mechanical force-assisted liquid exfoliation.[41] As shown in the TEM images (Figure 1a and b), WS_2 is delaminated into monolayer or few- flake layers and consequently forms multilayer stacks by controlling the initial concentration, sonication processing time and centrifugal speed. The d-spacing of 0.27 nm corresponding to the (100) plane of WS_2 is shown in the inset of in Figure 1c, which is consistent with the previous works.[42] The crystal structure of WS_2 in Figure 1d shows a hexagonal lattice, as confirmed by the diffraction characteristics in Figure S5. The high resolution transmission electron microscope (HRTEM) image and fast fourier transform (FFT) pattern presented in Figure 1d further confirm the successful formation of WS_2 nanosheets.

To identify the accumulating status of WS_2 nanosheets obtained by different processing methods, we performed the Raman spectroscopy characterization to study the number of the WS_2 flake layers. [30] The Raman spectra of the WS_2 flakes with different sonication processing time and centrifugal speed are shown in Figure 2. The typical WS_2 phonon modes: E^1 and A_{1g}, are expected to appear near 350.9 and 417.5 cm^{-1}, respectively.[43] As shown in Figure 2a, the Raman peaks at these two positions increase as the sonication time increases, indicating that more WS_2 flakes are exfoliated. On the other hand, the signal intensity of the WS_2 phonon modes decreases dramatically with increasing centrifugal speed (Figure 2b). Interestingly, the peaks at 323 cm^{-1} of the Raman spectrum of the film almost disappear after the treatment with a centrifugation speed of 8000 rpms, indicating that a monolayer or a bilayer WS_2 has been formed. [35]

To study the effects of substrate processing conditions on the change of WS_2 content on the substrate, the scanning electron microscopy (SEM) images of WS_2 films prepared on ITO with and without plasma treatment (Figure 3) were investigated. It is found that more WS_2 flakes are deposited on the surface of ITO without plasma treatment, while less WS_2 flakes adhere to the ITO surface treated by plasma (Figure 3a, b and d, e). By characterizing the Energy Dispersive X-ray Spectroscopy (EDS) and elemental map analysis of the WS_2 film, the concentration, work function and dispersion of the main elements on the surface can be revealed. [44] The results indicate that, compared with the case of the plasma-treated ITO, the sulfur (S) content of the WS_2 prepared on the ITO without plasma treatment is doubled, and the tungsten (W) content has also increased on untreated ITO, which confirms that more WS_2 flakes can be deposited on the ITO surface without plasma treatment (Figure 3c and f). The different deposition of WS_2 flakes on pristine ITO and plasma-treated ITO is likely affected by the varied chemisorption between WS_2 and these two ITO substrates as shown in Figure 6. Meanwhile, it can be seen from Figure 3 that although there are some discrete WS_2 flake aggregates, the WS_2 film deposited on the original ITO shows a higher yield, and at the same time it has a higher coverage and density, resulting in the better overall quality of the film.

The optical properties of HTLs also play a vital role in OSCs since the incident light needs to pass through this layer before it can be further absorbed by the active layer. Thus, we measured the transmission spectra of the devices with the configurations of ITO/WS**2**, ITO**plasma**/WS**2** and ITO/PEDOT: PSS, respectively (Figure 2c). WS**2** layer shows better transparency than PEDOT: PSS layer, especially in the 500 nm - 800 nm wavelength range where the energy distribution of the standard solar spectra is higher, which is beneficial for improving the ***JSC*** of the device. This can also provide a potentially high transmittance substrate for the further preparation of high-efficiency semitransparent OSCs.[45-47]

Device fabrication and characteristics

To evaluate the varying effects of the microstructure and physicochemical properties of WS**2** subjected to different processing methods, we first fabricated the devices based on J71: ITIC system by different processing conditions with the device structure of ITO/HTL/J71: ITIC/PDINO/Ag. The chemical structures and the energy levels of the different layers used in this study are shown in Figure 4a and 4b, respectively. By controlling the initial concentration, sonication time, centrifugal speed and thermal annealing to obtain the best WS_2 film as HTLs, the performance of the device has been significantly enhanced, especially the open-circuit voltage ***(VOC)*** (Table 1). Using the optimal WS_2 as the HTLs, the efficiency of the device is 4 times higher than that of the device with unoptimized WS**2** as the HTLs (9.25 % vs 2.07 %), and the device performance is comparable to that of using PEDOT: PSS as the HTLs. Through further research on work function (WF) of WS**2** film**,** we find that the obvious WF shift (from 5.33 eV to 5.78 eV, as shown in Figure S1 and Table 1) of WS**2** film leads to a contact barrier change between anode and active layer, which may be one of main reasons for the significant change of Voc. The reason why the work function of the WS_2 film in Table 1 increases with the increase of the ultrasonic time may be caused by the increased thickness of the WS_2 flake with a decreased mean nanosheet thickness, as confirmed in Figure S9.

To verify the versatility of the WS**2** interlayer obtained by the above processes, we used the more efficient PM6-Y6 system to fabricate OSCs via the device structure of ITO/HTL/PM6: Y6/PFN-Br/Ag. The photovoltaic parameters of the devices are summarized in Table 2 and the current density-voltage (J-V) characteristics are shown in Figure 4c. The best PCE of the devices fabricated on optimized WS_2 HTLs is 15.75%, which is even higher than that of the device with PEDOT: PSS as HTLs， as summarized in Table 2. The enhanced device performance can be attributed to a 8.3 % improvement of the short-circuit current (***JSC***). When the ITO substrate is treated with plasma for 3 minutes, the PCE of the devices using WS**2** as the HTL decreases from 15.75 % to 13.36 %, due to the simultaneous reduction of ***VOC***, ***JSC*** and fill factor (*FF*), which is consistent with the film properties as discussed previously. It is worth mentioning that the presence of some discrete aggregates in the WS_2 film may cause more leakage current. This is one of the reasons why higher dark currents are observed in WS_2-derived devices than PEDOT: PSS-derived devices in Figure S7. The ***JSC***s calculated from the external quantum efficiency (EQE) spectra are also consistent with that derived from photovoltaic performances (Figure 4d). The higher transmittance of the device with WS_2 can work together with the

better charge transfer performance of WS_2 layer to improve the EQE, which contributes to a higher J_{SC} of device. It is worth mentioning that the devices fabricated on WS_2 HTLs with plasma-treated ITO substrates perform differently from previous report,[33] probably caused by the different preparations of WS_2 film in this paper. In this work, we applied higher concentration and longer sonic processing time in the initial preparation to obtain the water-soluble WS_2 nanosheets. After that, the spin-coated WS_2 films were treated by thermal annealing at 60℃ for 5 mins. The morphology of the WS_2 films herein is quite different as compared with the previous report, which will be disscussed below by a series of morphology characterizations of WS_2 film.

To investigate the microstructure of the WS_2 films layers spun on untreated in-situ ITO and plasma-treated ITO substrates, we further conducted the grazing incident wide-angle X-ray scattering (GIWAXS) measurements, and the corresponding results are presented in Figure 5. Stronger scattering peaks from WS_2 films on untreated in-situ ITO are obviously observed in the out-of-plane direction than that on plasma-treated ITO, indicating a preferential orientation of WS_2 nanosheets parallel to the substrates, which is in favor of improving the conduction of the HTLs. Meanwhile, from the out-of plane linecuts, a higher intensity of the peak at around q=1.30 $Å^{-1}$ was observed for ITO/WS_2 film, compared with ITO**plamsa**/WS_2 film (Figure 5c), also indicating more ordered lamellar/layered packing structure of WS_2 nanosheets formed on untreated in-situ ITO[48]. This is consistent with the results of more **WS2** nanofalkes depositing to form a dense film as confirmed by the above-mentioned SEM measurement. Notably, we obtained improved stacking morphology of WS_2 film with higher conductivity by choosing the ITO without plasma treatment as substrate.

To gain more insight into morphology of the **WS2** layer, the surface morphologies of the active layers fabricated on different HTLs were characterized by AFM measurements under ambient conditions, as shown in Figure 6. The bright area is likely to be the distribution position of **WS2** flakes, while the relatively dark area represents the surface of ITO substrate. Figure 6(a) and (d) show that on the ITO surface that has not been treated by plasma, WS_2 flakes exhibit good dispersion and the film shows higher uniformity with a thickness about 3.48 ±2.00 nm according to the Gauss distribution statistics for the height of thin flakes (Figure S2). However, there are fewer WS_2 flakes deposited on the plasma-treated ITO surface, so the film uniformity is poor. This is in highly accordance with the deposition of WS_2 from the Figure 3. Moreover, the PM6:Y6 active layer spun on untreated in-situ ITO based WS_2 substrate appears more hydrophilic than on the device with plasma treated ITO, as revealed by the contact angle measurements as shown in Figure 6c, indicating that more Y6 may accumulate on the surface of active layer as Y6 is more hydrophilic than PM6 (Figure S3), which is beneficial for charge transport in the device. Considering that the surface energy of the substrate may affect the morphology of the active layer, [49,50] we further measured the surface morphology of active layer (PM6:Y6)(Figure 6b and e). The RMS of active layers on ITO/WS_2 and ITO**plasma**/WS_2 are 0.66 and 1.04 respectively, indicating that the surface morphology of the active layer become smoother when coated on ITO/WS_2 substrate as compared with that on ITO**plasma**/WS_2. Consequently, the above optimized WS_2 film

characteristics will not only facilitate the better charge extraction of the anode, but also are more conducive to the active layer deposition on the substrate to form a smoother film, which may be beneficial to the charge separation and transportation processes in the OSCs.

To elucidate the effects of optimized WS_2 HTLs on the device charge transport, charge mobility and extraction was investigated. The hole and electron mobilities of the devices were measured by the space charge limited current (SCLC) methods with the device structures of ITO (plasma or without plasma)/WS_2 or PEDOT: PSS/PM6: Y6/MoO_3/Ag and ITO/ZnO/ PM6: Y6/PFN-Br/Ag, respectively (Figure 7a). The hole mobilities of PM6:Y6 devices based on ITO**plasma**/PEDOT: PSS and ITO**plasma**/ WS_2 are 8.02×10^{-4} and 3.46×10^{-4} $cm^2V^{-1}s^{-1}$, respectively, while the hole mobility of PM6:Y6 devices based on ITO/WS_2 was increased to 1.97×10^{-3} $cm^2V^{-1}s^{-1}$, as summarized in Table S1. In addition, the work function of optimized WS_2 film was found to be 5.67 eV, as confirmed by ultraviolet photoelectron spectroscopy (UPS) measurement (Figure S4). Therefore, the significantly improved hole mobility could be attributed to the better film quality and higher conductivity of the WS_2 layer, which will further facilitate the charge transport in the devices given that the WF of the WS_2 film matches the HOMO energy level of the donor.

To study the charge recombination of OSCs with different HTLs, the correlation between J_{SC} and light intensity was further studied (Figure 7b). The correlation between J_{SC} and light intensity abides by the power law ($J_{sc} \propto I^{\alpha}$). The values of α of all the devices are close to 1, which indicates that monomolecular recombination dominates in these devices and the photo-generated charge carriers under short-circuit condition can be effectively extracted and collected by electrodes prior to recombination.[51,52] To investigate the charge carrier extraction of the devices, transient photovoltage (TPV) and transient photocurrent (TPC) measurements of the OSCs were performed, as shown in Figure 7c and d. The measurement data and specific fitting results of TPV and TPC of these devices are shown in Figure S10. Compared with the device using WS_2 interlayer formed on in-situ ITO, as summarized in Table S2, the charge lifetime of the device using WS_2 interlayer prepared on plasma-treated ITO as HTL is significantly reduced from 3.95 μs to 1.03 μs, while the charge extraction time increases from 0.65 μs to 0.74 μs, indicating that a more severe charge recombination and reduced charge extraction capacity in the device. This is again consistent with the film properties and the devices performance as discussed above.

Conclusions

In summary, the high-yield and high-quality liquid exfoliated WS_2 nano-flaky layers are successfully fabricated on ITO and used as solution-processed HTLs in highly efficient PM6:Y6 Non-fullerene OSCs. We find that by depositing the high-quality WS_2 suspension obtained after comprehensive optimization factors such as concentration, ultrasonication time and centrifugal speed, onto the ITO as an interlayer, the work function of the composite substrate can be made greater than that of PEDOT:PSS. An improved energy level alignment between the substrate and the active layer thus leads to better charge transport in the device, as revealed by the charge transportation

characteristics in the OSCs. The GIWAXS, TEM, SEM and elemental mapping results show that the conductivity, coverage and uniformity of the WS_2 flakes spin-coated on untreated in-situ ITO are improved compared to that of plasma- treated ITO. As a result, the PM6:Y6 BHJ-based OSCs with the above-mentioned multiple optimized WS_2 layer as the HTLs produce a maximum PCE of 15.75%, which is higher than the value of the PEDOT-PSS based control devices (15.31%). The morphological characteristics and carrier recombination process studies show that the improvement of OSCs performance can be attributed to the enhanced charge transport and the reduced bimolecular recombination due to the high quality interlayer. Therefore, this work provides a useful strategy for preparing high-yield and high-quality TMD as HTLs in efficient OSCs and other optoelectronics devices.

Experimental

Materials

WS_2 powder (3250-12500mesh;>99.9% purity) was obtained from ZhongNuo Advanced Material (Beijing)Technology Co., Ltd. Poly(3,4-Athylenedioxythiophene)poly(styrenesulfonate)(PEDO T: PSS) was purchased from H.C starck Inc (CLEVIOS P VP AI 4083). Poly(1-(5-(4,8-bis(5-(2-ethylhexyl)-4-fluorothiophen-2-yl) benzo[1,2-b:4,5-b 0]dithiophen-2-yl)thiophen-2-yl)-5,7-bis(2-ethylhexyl)-3-(thiophen-2-yl)-4H,8H-benzo[1,2-c:4,5-c0]dithiop hene-4,8-dione) (PM6),(2,20-((2Z,20Z)-((12,13-bis(2-ethylhexyl)-3,9-diundecyl-12,13-dihydro[1,2,5]thiadiazolo[3,4-e]thieno[2," 30':4',50]thieno[20,30:4,5]pyrrolo[3,2-g]thieno[20,30:4,5]thieno[3, 2-b]indole-2,10-diyl)bis(methany-lylidene))bis(5,6-difluoro-3-oxo- 2,3-dihydro-1H-indene-2,1-diylidene)) dimalononi trile) (Y6)， 3,9 - bis(2 - methylene - (3 - (1,1 - dicyanomethylene) - indanone)) - 5,5,11,11 - tetrakis(4 - hexylphenyl) - dithieno[2,3-d:2' ,3' -d'] - s - indaceno[1,2 - b:5,6 - b']dithiophene) (ITIC), (poly[(9,9-bis(30-((N,N-dimethyl)-N- ethylammonium)-propyl)-2,7fluorene)-alt-2,7-(9,9-dioctylfluo rene)] dibromide) (PFN-Br), (N,N-dimethyl-ammonium N-oxide)propyl perylene diimide (PDINO) were purchased from Solarmer Cop. poly[(4,8-bis(5-(tripropylsilyl)thiophen-2-yl) benzo[1,2-b:4,5-b']dithiophene)-co-(5,6-difluoro-2-(2-hexyldecyl)-4,7-di(thiophen-2-yl)-2H-benzo[d][1,2,3]triazole)] (J71) was purchased from VIZUchem Co,Ltd. Other chemicals or materials were purchased from the relevant companies.

Preparation of WS2 nanosheets with different sizes

WS_2 powder was added in a mixture solution containing deionized water and ethanol (1:1 v/v) with concentrations of 6 to 14 mg mL^{-1}. To prepare small size WS_2 solution, the blend solutions were treated with probe sonication under 5 ℃ water bath for 6-12 h (750 W, automatic amplitude). The unexfoliated WS2 was removed by centrifuging the cloudy solutions to the speed of 4000 - 8000 rpm for 30 mins. After centrifugation, the light-yellow transparent supernatant was collected for further operation.

Device fabrication

To begin this process, glass/ITO substrates were cleaned in an ultrasonic water bath with a diluted detergent solution, deionized water, and isopropanol, respectively. The ITO dried at 70 °C were treated with O_2-plasma for 3 minutes, or directly used without

plasma treatment. A PEDOT:PSS solution was spun onto the ITO substrates at 3000 rpm for 30 s, followed by 15 min annealing at 150 ℃. For the HTL of WS_2, WS_2 solution was spin coated on ITO substrates at 900 rpm for 30 s, and the samples were quickly transferred to heating plate at 60 ℃ for 5 min. The J71: ITIC with 1:1 weight ratio (total 20 mg mL^{-1}) was dissolved in chloroform. The PM6:Y6 was prepared with ratio 1:1.2 (total 16 mg mL^{-1}) in chloroform containing 0.5% volume of the 1-chloronaphthalene solvent. All the solution of active layer were spin-coated onto the HTLs at 3000 rpm for 40 s. A thin ETL (electron transport layer) of PDINO (1 mg mL^{-1} in methanol) was spun on top of J71: ITIC at 3000 rpm for 40 s. A thin ETL of PFN-Br (0.5 mg mL^{-1} in methanol) was spun on top of PM6:Y6 at 3000 rpm for 40 s. The devices were completed by depositing 100 nm Ag top electrode under vacuum (3×10^{-4} Pa) with a shadow mask. Typical cells have devices area of 5.7 mm^2.

Characterizations

The morphologies of the as-prepared WS_2 nanosheets and HTLs were observed by atomic force microscopy (AFM, Innova), field emission scanning electron microscopy (SEM, Merlin) and transmission electron microscopy (TEM, JEM 2100F). The contact Angle was tested using DSA-X (Guangzhou, Beto Science and Technology Co., Ltd.). Raman spectroscopic analysis was detected by a Renishaw Invia-428K38 micro laser Raman tester, with a 523 nm laser source. The UV-vis transmittance of HTLs was measured by Lambda 365 (PerkinElmer). The Ultraviolet photoelectron spectroscopy was measured by atmospheric photoelectron spectrometer AC-3(RIKEN Instrument Co.,Ltd.). The current density-voltage (J-V) characteristics were collected using Keithley 2400 Source in AM 1.5G spectrum from solar simulator. The light intensity for the J-V measurements was adjusted with a reference silicon cell (Hamamatsu S1133 certified by National Renewable Energy Laboratory). EQE test system for spectra characterization was purchased from Enli Technology Co., Ltd. The transient photovoltage (TPV) and transient photocurrent (TPC) techniques were based in customized transient measurement systems with a Q-Smart100 nanosecond pulse laser. The film thickness was measured using the DEKTAK 150 Step Profiler. The carrier mobility of the hole- only devices (electron-only devices) was extracted by fitting the voltage via space charge limited current (SCLC). The equation from Mott-Gurney square law is as follows: $J=9\varepsilon_r\varepsilon_0\mu V^2/8d^3$ where ε_r is the relative dielectric constant, ε_0 is the permittivity of vacuum, d is the thickness of the active layers, uh (ue) is the hole (electron) mobility. The grazing incident wide-angle X-ray scattering (GIWAXS) measurements were performed at Xenocs (France). The wavelength of X-ray source was set to 1.34144 Å and the incident angle was 0.2°. The X-ray diffraction (XRD) measurements were performed using X'pert Powder (PANalytical) at 300K. The 2θ range from 10 to 80° in step of 0.013° with a count time of 1 s. The X-ray Photoelectron Spectroscopy (XPS) were performed at Thermo Fisher ESCALAB XI+ (United Kingdom). The high-resolution XPS analysis of C 1s, In 3d, Sn 3d spectra is shown in Figure S6, Supporting Information.

Conflicts of interest

There are no conflicts to declare.

Acknowledgements
The authors thank the Guangdong International Science and Technology Cooperation Foundation (2020A0505100002), the National Key Research and Development Program of China (2017YFA0206600), the National Natural Science Foundation of China (21733005, 51861145301), Guangdong Special Support Program (2017TQ04N559), Guangdong-Hong Kong-Macao Joint Laboratory of Optoelectronic and Magnetic Functional Materials (2019B121205002) and the Hong Kong Polytechnic University (1-ZE1C).

Notes and references

1 Q. Wang, Y. Xie, F. Soltani-Kordshuli and M. Eslamian, *Renewable Sustainable Energy Rev*, 2016, **56**, 347–361.
2 K. Gao, J. S. Miao, L. G. Xiao, W. Y. Deng, Y. Y. Kan, T. X. Liang, C. Wang, F. Huang, J. B. Peng, Y. Cao, F. Liu, T. P. Russell, H. B. Wu and X. B. Peng, *Adv. Mater.*, 2016, **28**, 4727–4733.
3 Y. Cui, H. F. Yao, J. Q. Zhang, K. H. Xian, T. Zhang, L. Hong, Y. M. Wang, Y. Xu, K. Q. Ma and C. B. An, *Adv. Mater.*, 2020, **32**, 1908205.
4 Q. Liu, Y. Jiang, K. Jin, J. Qin, J. Xu, W. Li, J. Xiong, J. Liu, Z. Xiao, K. Sun, S. Yang, X. Zhang and L. Ding, *Sci. Bull.,* 2020, **65**, 272.
5 Y. Lin, Y. Firdaus, F. H. Isikgor, M. I. Nugraha, E. Yengel, G. T. Harrison, R. Hallani, A. El-Labban, H. Faber, C. Ma, X. Zheng, A. Subbiah, C. T. Howells, O. M. Bakr, I. McCulloch, S. D. Wolf, L. Tsetseris and T. D. Anthopoulos, *ACS Energy Letters,* 2020, **5**, 2935-2944.
6 Y. Lin, M. I. Nugraha, Y. Firdaus, A. D. Scaccabarozzi, F. Aniés, A.-H. Emwas, E. Yengel, X. Zheng, J. Liu, W. Wahyudi, E. Yarali, H. Faber, O. M. Bakr, L. Tsetseris, M. Heeney and T. D. Anthopoulos, *ACS Energy Letters,* 2020, **5**, 3663-3671.
7 M. B. Salim, R. Nekovei and R. Jeyakumar, *Solar Energy,* 2020, **198**, 160-166.
8 Y. Cui, H. Yao, J. Zhang, K. Xian, T. Zhang, L. Hong, Y. Wang, Y. Xu, K. Ma, C. An, C. He, Z. Wei, F. Gao and J. Hou, *Adv Mater.,* 2020, **32**, 1908205.
9 X. J. Wang, Y. D. Yang, Z. C. He, H. B. Wu and Y. Cao, *J. Mater. Chem. C,* 2019, **7**, 14861-14866.
10 M. Graetzel, R. A. J. Janssen, D. B. Mitzi and E. H. Sargent, *Nature,* 2012, **488**, 304–312.
11 L. L. Zhan, S. X. Li, T. K. Lau, Y. Cui, X. H. Lu, M. M. Shi, C. Z. Li, Li, H. Y. J. H. Hou, H. Z. Chen and H. Z. Chen, *Energy & Environmental Science,* 2020, **13**, 635-645.
12 J. Yuan, Y. Zhang, L. Zhou, G. Zhang, H.-L. Yip, T.-K. Lau, X. Lu, C. Zhu, H. Peng, P. A. Johnson, M. Leclerc, Y. Cao, J. Ulanski, Y. Li and Y. Zou, *Joule,* 2019, **3**, 1140.
13 Y. Cui, H. F. Yao, L. Hong, T. Zhang, Y. B. Tang, B. J. Lin, K. H. Xian, B. W. Gao, C. B. An, P. Q. Bi, W. Ma and J. H. Hou, *National Science Review,* 2020, **7**, 1239-1246.
14 E. F. He, X. J. Wang, Y. Lu, Y. L. Yin, F. Y. Guo, S. Y. Gao, Z. C. He, L. C. Zhao, Y. Cao and Y. Zhang, *ACS Applied Energy Materials,* 2020, **3**, 6133-6138.
15 G. T. Chen, G. H. Qian, S. W. Yi, Z. C. He, H.B. Wu, W. Yang, B.

Zhang and Y. Cao, *ACS Appl. Mater. Interfaces,* 2019, **11**, 45969–45978.
16 X. J. Wang, S. W. Yi, Z. C. He, X. H. Ouyang, H. B. Wu, W. G. Zhu, B. Zhang and Y. Cao, *Sustain. Energ. Fuels,* 2020, **4**, 1234.
17 M. Zeng, X. Wang, R. Ma, W. Zhu, Y. Li, Z. Chen, J. Zhou, W. Li, T. Liu, Z. He, H. Yan, F. Huang and Y. Cao, *Advanced Energy Materials,* 2020, **10**, 2000743.
18 C. Feng, X. J. Wang, Z. C. He and Y. Cao, *Solar RRL*, 2021, **5**, 2000753.
19 C. Feng, X. J. Wang, G. T. Chen, B. Zhang, Z. C. He and Y. Cao, Langmuir, 2021, **37**, 4347-4354.
20 M. Sun, H. Zhang, C. Liang, C. Ji, X. Jing, F. Sun, Q. Song, F. You and Z. He, *Advanced Materials Interface*s, 2020, **7**, 2000412.
21 M. Nam, S. Baek and D.-H. Ko, *Applied Surface Science,* 2020, **526**, 146632.
22 G. Long, X. Wan, B. Kan, Z. Hu, X. Yang, Y. Zhang, M. Zhang, H. Wu, F. Huang, S. Su, Y. Cao and Y. Chen, *ChemSusChem,* 2014, **7**, 2358-2364.
23 L. Y. Su, H. H. Huang, Y. C. Lin, G. L. Chen, W. C. Chen, W. Chen, L. Wang and C. C. Chueh, *Advanced Functional Materials*, 2021, **31**, 2005753.
24 P. C. Lin, Y. T. Wong, Y. A. Su, W. C. Chen and C. C. Chueh, *ACS Sustainable Chem. Eng.*, 2018, **6**, 14621-14630.
25 D. Alemu, H. Y. Wei, K. C. Ho and C. W. Chu, *Energy Environ. Sci*., 2012, **5**, 9662.
26 P. K. Giesbrecht, J. P. Bruce and M. S. Freund, *ChemSusChem,* 2016, **9**, 109-117.
27 A. R. Tapa, W. C. Xiang, A. S. A. Ahmed, S. W. Wu, B. Li, Q. F. Liu, C. M. J. Chui and X. J. Zhao, *Materials Chemistry Frontiers,* 2021, **5**, 2702-2714.
28 L. Chen, C. Xie and Y. W. Chen, *Adv. Funct. Mater*., 2014, **24**, 3986.
29 M. De Jong, L. Van Ijzendoorn and M. De Voigt, *Appl. Phys. Lett.,* 2000, **77**, 2255.
30 Z. Zhao, Q. Wu, F. Xia, X. Chen, Y. Liu, W. Zhang, J. Zhu, S. Dai and S. Yang, *ACS Appl. Mater. Interfaces,* 2015, **7**, 1439.
31 Q. S. Wei, M. Mukaida, Y. Naitoh and T. Ishida, *Adv. Mater*., 2013, **25**, 2831.
32 X. Yu, T. J. Marks and A. Facchetti, *Nat. Mater*., 2016, **15**, 383.
33 Y. Lin, B. Adilbekova, Y. Firdaus, E. Yengel, H. Faber, M. Sajjad, X. Zheng, E. Yarali, A. Seitkhan, O. M. Bakr, A. El-Labban, U. Schwingenschlögl, V. Tung, I. McCulloch, F. Laquai and T. D. Anthopoulos, *Advanced Materials,* 2019, **31**,1902965.
34 K. G. Zhou, N. N. Mao, H. X. Wang, Y. Peng and H. L. Zhang, *Angew. Chem., Int. Ed*., 2011, **50**, 10839.
35 P. K. Chow, E. Singh, B. C. Viana, J. Gao, J. Luo, J. Li, Z. Lin, A. L. Elías, Y. Shi, Z. Wang, M. Terrones and N. Koratkar, *ACS Nano,* 2015, **9**, 3023-3031.
36 Y. -J. Huang, P.-J. Yen, H.-C. Wang, H.-C. Chen and K.-H. Wei, *Organic Electronics,* 2019, **72**, 6-17.
37 P. Nuchuay, W. Promcham1, C. Laongwan, T. Chaikeeree, S. Limwichean, P. Eiamchai, V. Pattantsetakul, N. Nuntawong, C. Chananonnawathorn, C. Oros, P. Songsirirtthigul and M. Horprathum, *AIP Conference Proceedings,* 2020, **2279**, 120010.

38 C. C. Lee, R. C. Shih, P. C. Huang and S. F. Tseng, *Surface & Coatings Technology*, 2020, **388**, 125601.
39 B. B. Sahu, M.W. Lee, W. Long and J. G. Han, *Aip Advances,* 2020, **10**, 105 231.
40 G. Gopakumar, S. V. Nair and M. Shanmugam, *Nanoscale,* 2020, **12**, 239-247.
41 X. Zhang, H. Cheng and H. Zhang, *Adv. Mater.,* 2017, **29**, 1701704.
42 Y. Yue, J. Chen, Y. Zhang, S. Ding, F. Zhao, Y. Wang, D. Zhang, R. Li, H. Dong, W. Hu, Y. Feng and W. Feng, *ACS Appl Mater Interfaces,* 2018, **10**, 22435-22444.
43 F. Wang, I. A. Kinloch, D. Wolverson, R. Tenne, A. Zak, E. O'Connell, U. Bangert and R. J. Young, *2D Materials,* 2016, **4**, 015007.
44 F. Mousavi, M. Shamsipur, A. Taherpour and A. Moghimi, Materials Science in Semiconductor Processing, 2021, **123**, 105468.
45 C. Sun, R. Xia, H. Shi, H. Yao, X. Liu, J. Hou, F. Huang, H. L. Yip and Y. Cao, *Joule,* 2018, **2**, 1816-1826.
46 R. Xia, H. Gu, S. Liu, K. Zhang, H. L. Yip and Y. Cao, *Solar RRL,* 2019, **3**, 1800270.
47 Y. Xie, Y. Cai, L. Zhu, R. Xia, L. Ye, X. Feng, H. L. Yip, F. Liu, G. Lu, S. Tan and Y. Sun, *Advanced Functional Materials,* 2020, **30**, 2002181.
48 R. Mastria, R. Scarfiello, D. Altamura, C. Giannini, A. Liscio, A. Kovtun, G. V. Bianco, G. Bruno, V. Grillo, A. H. Tavabi, R. E. Dunin-Borkowski, C. Nobile, A. Cola, P. D. Cozzoli, S. Gambino and A. Rizzo, *Sci Rep*, 2019, **9**, 9002.
49 H. Yano, D. Kouro, N. Sasaki and S.-i. Muramatsu, *Solar Energy Materials and Solar Cells,* 2009, **93**, 976-979.
50 A. B. Djurišić, C. Y. Kwong, P. C. Chui and W. K. Chan, *Journal of Applied Physics,* 2003, **93**, 5472-5479.
51 S. Song, K. T. Lee, C. W. Koh, H. Shin, M. Gao, H. Y. Woo, D. Vak and J. Y. Kim, *Energy Environ. Sci.,* 2018, **11**, 3248-3255.
52 W. Chen, G. Huang, X. Li, H. Wang, Y. Li, H. Jiang, N. Zheng and R. Yang, *ACS Appl. Mater. Interfaces*, 2018, **10**, 42747-42755.

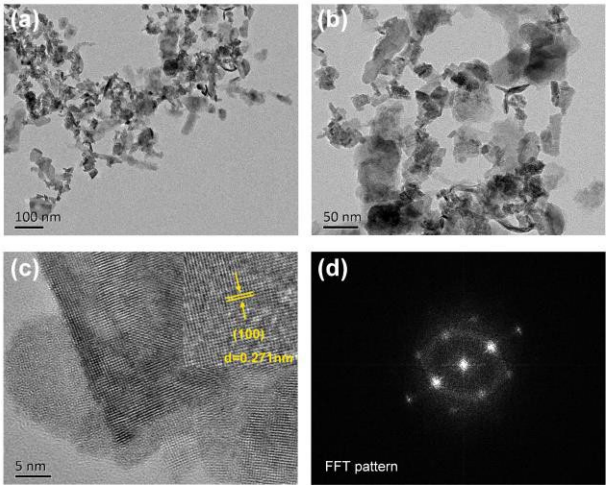

Figure 1. (a, b) TEM images of WS_2 nanosheets (c) HRTEM images. Inset in (c) shows the lattice domain. (d) The corresponding Fast Fourier Transform (FFT) pattern of the lattice.

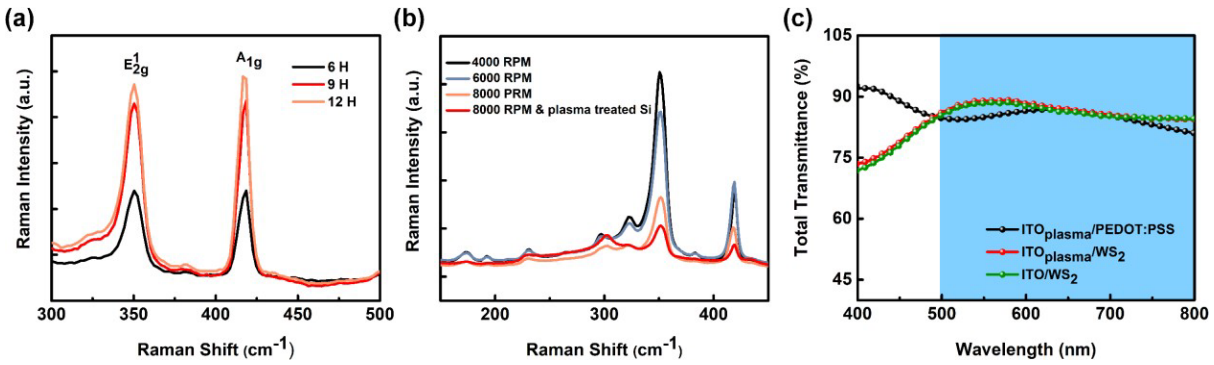

Figure 2. (a) Raman spectra subjected to different sonic processing time, ranging from 6 to 12 hrs for WS_2 films on Si substrates. (b) Raman spectra of device subjected to different centrifugal speeds, ranging from 4000 to 8000 rpms, and with plasma treatment. (c) Transmittance spectra of ITO_{plasma}/PEDOT: PSS, ITO_{plasma}/WS_2 and ITO/WS_2.

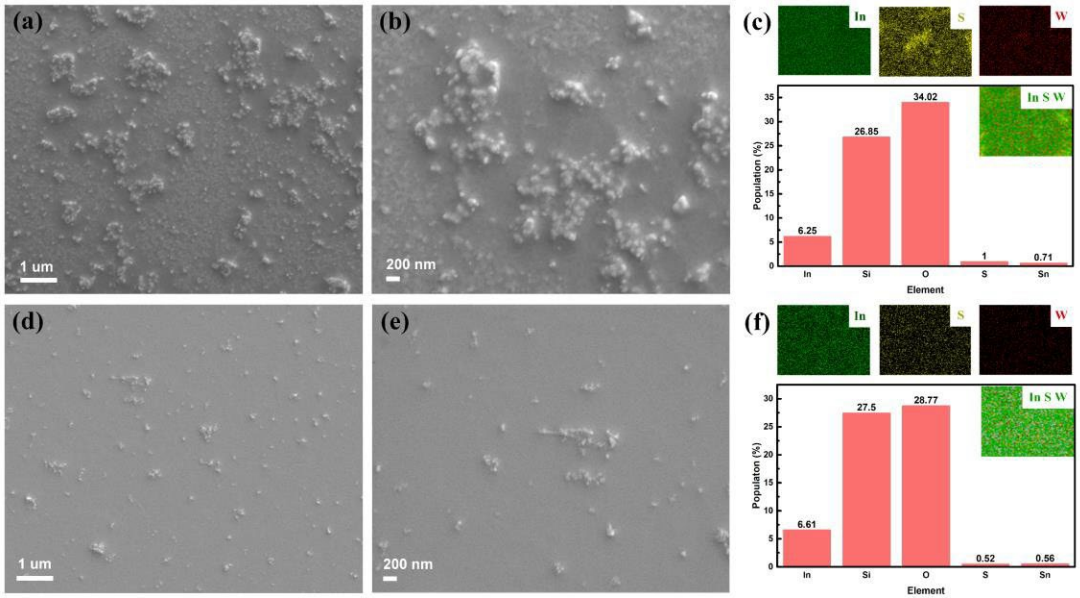

Figure 3. SEM images of (a, b) ITO/WS_2 and (d, e) ITO_{plasma}/WS_2, in company with (c, f) the corresponding elemental content and EDS maps.

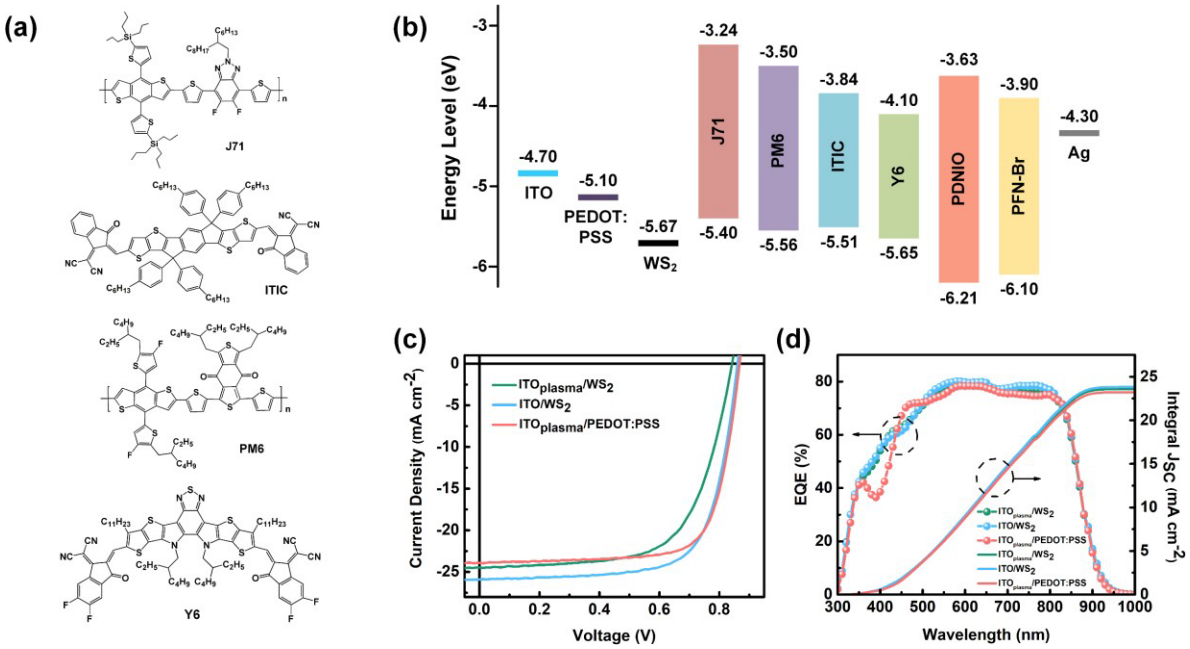

Figure 4. (a) The chemical structures of the active layer materials. (b) The corresponding energy level diagrams. (c) The J-V characteristics of the devices under 100 mW cm^{-2} air mass 1.5 globe (AM1.5G) irradiation. (d) EQE spectra of the OSCs.

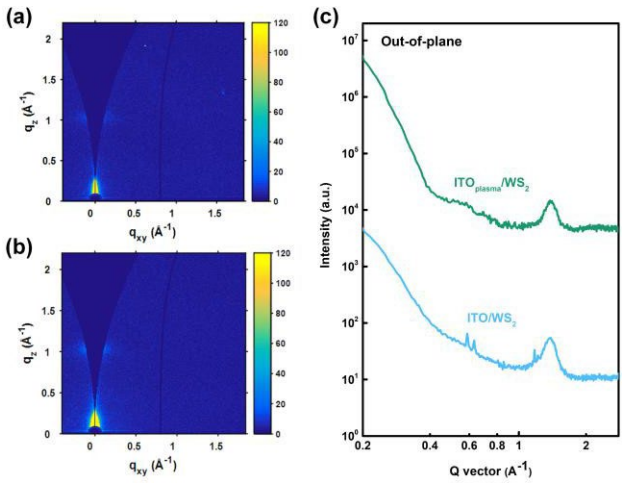

Figure 5. 2D GIWAXS patterns of (a) ITO_{plasma}/WS_2 and (b) ITO/WS_2, and (c) the correspongding 1D line-cuts in the out of plane.

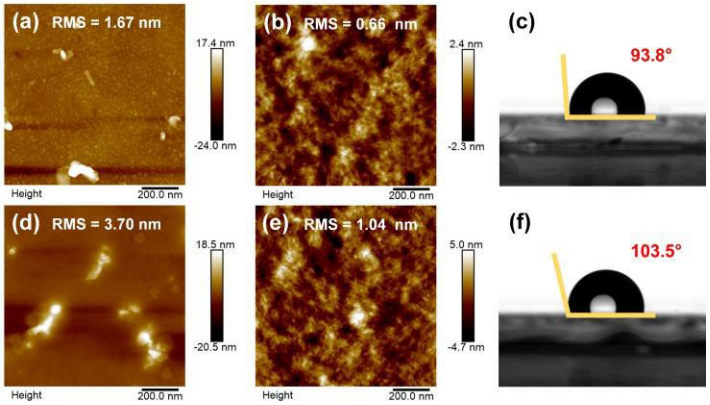

Figure 6. AFM images of (a) ITO/WS_2 and (d) ITO_{plasma}/WS_2, AFM images and photographs of water droplets on the surfaces of the PM6:Y6 film formed on (b, c) ITO/WS_2, (e, f) ITO_{plasma}/WS_2.

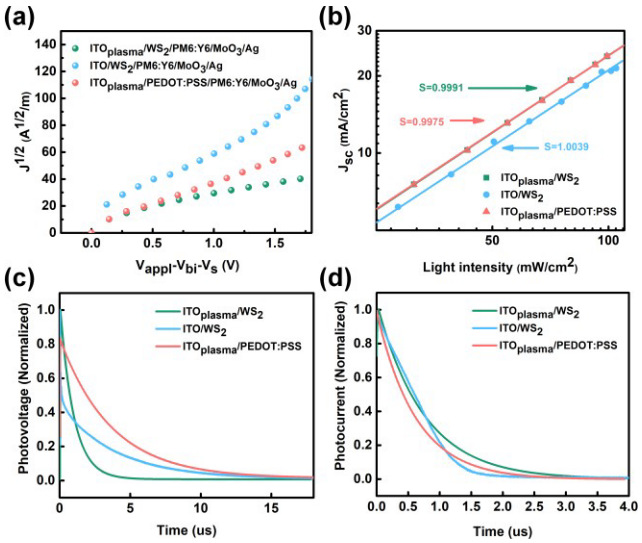

Figure 7. (a) The SCLC curves of hole- only devices. (b) The light intensity-dependent J_{sc} and (c, d) TPV and TPC of devices based on three modified anodes:ITO/WS_2,ITO_{plasma}/WS_2 and ITO_{plasma}/PEDOT: PSS.

Table 1. The photovoltaic parameters of J71: ITIC based OSCs with WS_2 films as HTLs prepared via different processing conditions.

HTL	Initial concentration (mg/mL)	Sonic processing time (h)	Voc (V)	Jsc (mA cm^{-2})	FF (%)	PCE best.(%)	WF (eV)
WS_2[a]	6	6	0.38	13.99	38.41	2.07(1.68)[c]	5.33
	6	9	0.50	14.07	47.17	3.34(2.95)[c]	5.50
	6	12	0.57	14.37	47.06	3.87(3.29)[c]	5.78
WS_2[b]	6	9	0.68	16.17	45.33	5.00(4.53)[c]	5.50
	10	9	0.93	15.65	59.23	8.63(8.22)[c]	5.65
	14	9	0.92	17.63	57.10	9.25(8.77)[c]	5.67

[a] As-cast. [b] With thermal annealing at 60 ℃ for 5 min.[c] Average PCE value of 20 independent devices.

Table 2. The photovoltaic parameters of the PM6: Y6 based OSCs with different HTLs.

HTL	Voc (V)	Jsc (mA cm^{-2})	FF (%)	PCE best. (%)	PCE avg. (%)[c]
WS_2[a]	0.84	24.46	64.82	13.35	12.91
WS_2[b]	0.86	25.90	70.65	15.75	15.52
PEDOT:PSS	0.87	23.91	73.80	15.31	15.21

[a] ITO with plasma treatment. [b] ITO without plasma treatment. [c] Average PCE value of 20 independent devices.